Comparison of Pulsed Three-Dimensional CEST Acquisition Schemes at 7 Tesla: Steady State Versus Pseudosteady State

Vitaliy Khlebnikov,[1]* Nicolas Geades,[2] Dennis W. J. Klomp,[1] Hans Hoogduin,[1] Penny Gowland,[2] and Olivier Mougin[2]

Purpose: To compare two pulsed, volumetric chemical exchange saturation transfer (CEST) acquisition schemes: steady state (SS) and pseudosteady state (PS) for the same brain coverage, spatial/spectral resolution and scan time.

Methods: Both schemes were optimized for maximum sensitivity to amide proton transfer (APT) and nuclear Overhauser enhancement (NOE) effects through Bloch-McConnell simulations, and compared in terms of sensitivity to APT and NOE effects, and to transmit field inhomogeneity. Five consented healthy volunteers were scanned on a 7 Tesla Philips MR-system using the optimized protocols at three nominal B_1 amplitudes: 1 μT, 2 μT, and 3 μT.

Results: Region of interest based analysis revealed that PS is more sensitive ($P < 0.05$) to APT and NOE effects compared with SS at low B_1 amplitudes (0.7–1.0 μT). Also, both sequences have similar dependence on the transmit field inhomogeneity. For the optimum CEST presaturation parameters (1 μT and 2 μT for APT and NOE, respectively), NOE is less sensitive to the inhomogeneity effects (15% signal to noise ratio [SNR] change for a B_1 dropout of 40%) compared with APT (35% SNR change for a B_1 dropout of 40%).

Conclusion: For the same brain coverage, spatial/spectral resolution and scan time, at low power levels PS is more sensitive to the slow chemical exchange-mediated processes compared with SS. **Magn Reson Med 77:2280–2287, 2017.**

Key words: CEST; APT; NOE; volumetric CEST sequence; steady state; pseudosteady state

INTRODUCTION

Chemical exchange saturation transfer (CEST) has been used extensively to measure low concentration solutes through exchange of labile protons with water detected by means of the z-spectrum (1,2). Two particularly prominent z-spectrum features are amide proton transfer (APT) and nuclear Overhauser enhancement (NOE) related peaks, both of which are believed to originate from endogenous mobile proteins and peptides localized in the cellular cytosol. APT is associated with mobile protein content (3–5) and is pH dependent (6–8), whereas the NOE effect has been reported to be linked to tissue cellularity (9) and cellular membrane fluidity (10). The sensitivity to both features is highly sequence dependent.

Z-spectrum imaging ideally uses three-dimensional (3D) acquisitions to provide whole brain coverage at high sensitivity and two 3D acquisition schemes are currently described in literature. Both are pulsed saturation techniques which can operate well within amplifier duty cycle and specific absorption rate limitations, and can be used to provide high resolution images in a reasonable time. The first is based on the standard magnetization transfer (MT) imaging technique: a steady-state (SS) acquisition alternating brief periods of saturation and image acquisition (11,12). The second prepares the magnetization with a prolonged saturation before an extended readout period, where the prolonged saturation achieves a pseudosteady state (PS) before the image acquisition (13,14).

The aim of this study was to compare the SS and PS approaches for the same brain coverage, spatial/spectral resolution and scan time. First, simulations based on a four-pool Bloch-McConnell model (15) were used to optimize both sequences for maximum sensitivity to APT and NOE effects, considering the number of saturation pulses, transmit field amplitude and duty cycle. Second, the optimized SS and PS protocols were systematically compared in terms of the sensitivity to APT and NOE, and to transmit field inhomogeneity. This study provides a framework for the rational choice of pulsed 3D z-spectrum acquisition scheme.

METHODS

The SS and PS 3D CEST sequences used are shown in Figure 1. The SS sequence (Fig. 1A) consists a single, short, off-resonance, presaturation radiofrequency (RF) pulse (applied at a specific frequency offset relative to water), a crusher gradient to destroy residual magnetization in x–y plane and a segmented 3D echo planar imaging (EPI) readout. This module is repeated at a relatively short repetition time (TR).

[1]Department of Radiology, University Medical Center Utrecht, Utrecht, the Netherlands.

[2]Sir Peter Mansfield Imaging Center, School of Physics and Astronomy, University of Nottingham, Nottingham, Nottinghamshire, United Kingdom.

Grant sponsor: the European Commission under FP7 Marie Curie Actions; Grant numbers: FP7-PEOPLE-2012-ITN-316716.

*Correspondence to: Vitaliy Khlebnikov, MSc, University Medical Center Utrecht, Department of Radiology, Heidelberglaan 100, Q.02.4.308, Utrecht, 3584 CX, the Netherlands; E-mail: v.khlebnikov@umcutrecht.nl

Received 2 February 2016; revised 31 May 2016; accepted 5 June 2016

DOI 10.1002/mrm.26323

Published online 25 July 2016 in Wiley Online Library (wileyonlinelibrary.com).

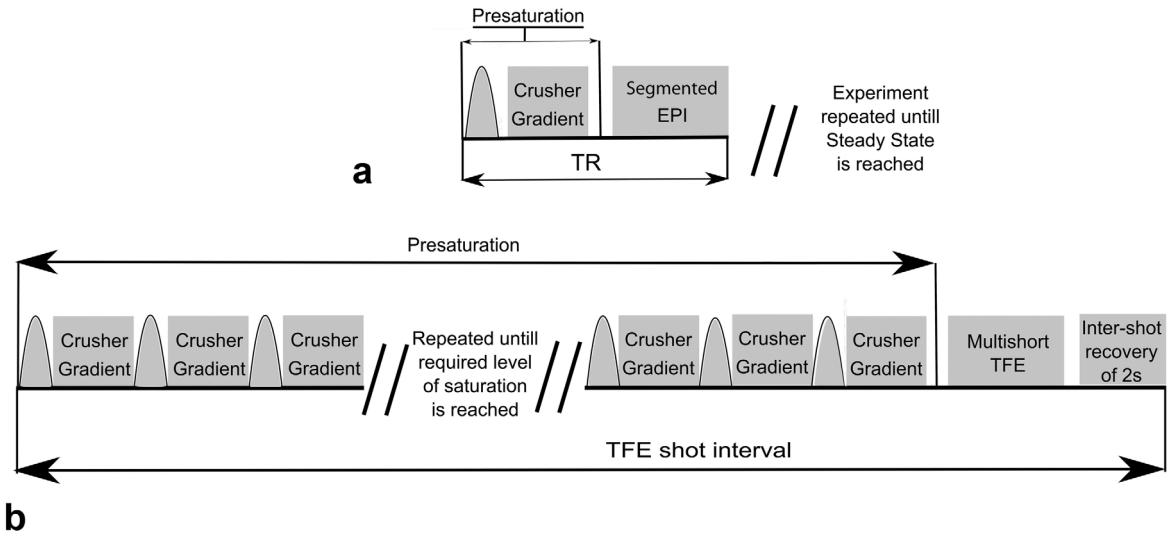

FIG. 1. A schematic of the compared pulsed 3D CEST sequences: SS image acquisition (**A**) and PS image acquisition (**B**).

Suppression of the water's longitudinal magnetization due to exchange competes with its T1-relaxation (T1w) during the delay between the saturation and the readout. The SS magnetization is built up over the multiple sequence repetitions, with the rate of build-up of saturation being governed by tissue T1w. k-space is sampled from high to low spatial frequencies so that the center of k-space is sampled when the SS has been established. The PS sequence (Fig. 1B) consists of a train of short, off-resonance, presaturation RF pulses (applied at a specific frequency offset relative to water), a crusher gradient for destroying residual transverse magnetization and a segmented 3D turbo factor (TFE) readout with a delay of 2 s for T1w recovery to increase the signal-to-noise ratio (SNR). The number of pulses in the train determines the level of saturation. Competition between suppression and longitudinal recovery of the water's longitudinal magnetization occur during the time between saturation pulses.

Data acquisition starts in the center of k-space to maximize sensitivity to the saturation. The relationship between flip angle (FA) and sensitivity depends on the SS longitudinal magnetization at the end of each readout train, the subsequent suppression of the longitudinal magnetization at the start of the readout train and the readout FA. Therefore, in general the optimum FA will be higher than the Ernst angle. However, a high FA creates a rapid evolution of signal at the start of k-space and hence a broadened point spread function. After two dummy acquisitions, phase encoding is applied radially to sensitize the center of k-space to the preparation steps. Three shots of the sequence shown in Figure 1B are required to reach PS.

Numerical Simulations

Both SS and PS CEST techniques were optimized for maximum sensitivity to APT and NOE effects through Bloch-McConnell equation simulations (15). The following sequence parameters were investigated: the number of saturation pulses (saturation time), transmit field amplitude and duty cycle. Gradient (GR) and RF spoiling was simulated by setting the transverse magnetization components to 0. All other sequence parameters are the same as for data acquisition (see the Data Acquisition section below).

Four-pool (water, APT, NOE, and super-lorentzian lineshape MT) Bloch-McConnell equations were solved numerically (16) assuming white matter parameters (Table 1) similar to those reported in Mougin et al (14). The T1 values of all pools other than water were fixed to 1 s (17). This model assumes that there are only four pools in the system and that the only interactions are with water. APT (amplitude at 3.5 ppm) and NOE (amplitude at -3.5 ppm) effect sizes (contributions to the z-spectrum) were quantified by the pool difference method:

$$APT = S(3.5ppm, M_A = 0) - S(3.5ppm, M_A = 1) \quad [1]$$

where *APT* is the effect size of APT, $S(\Delta\omega,MA)$ is the simulated signal in the z-spectrum at $\Delta\omega = 3.5$ ppm, and *MA* is the simulated amplitude of the APT compartment. A similar expression can be written for *NOE* effect size at $\Delta\omega$ = -3.5 ppm. The sensitivity to APT or NOE can be calculated as follows (18):

$$SNR_{APT} = \frac{APT}{\sqrt{2}} SNR_{Io} \quad [2]$$

where APT is defined in Eq. [1] and *SNRIo* is the SNR of the control scan which is further defined for the gradient field echo readout as:

$$SNR_{Io} = \frac{I_{norm}}{Noise} \quad [3]$$

Table 1
White Matter Parameters Used in the Bloch-Mcconnell Simulations.[a]

	Water	APT	NOE	MT
T_1 (s)	1.2	1	1	1
T_2	40 ms	10 ms	0.3 ms	10 μs
$\Delta\omega$ (ppm)	0	3.5	-3.5	0
M_0 (%)	-	0.15	6	11
R (Hz)	-	50	10	50

[a]White matter parameters used in the Bloch-McConnell simulations were based on Mougin et al (14).

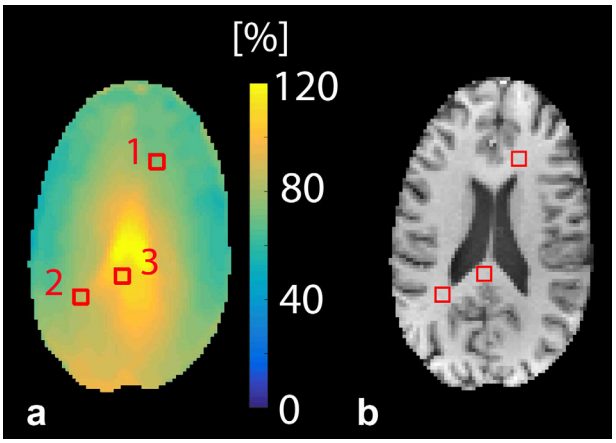

FIG. 2. Example ROIs (100 mm^2) drawn on a single slice of B_1 map (%) (**a**) and T_1-weighted image (**b**) of a healthy subject. Care was taken to position ROIs in similar locations for all five subjects in this study.

where *Inorm* is the normalization signal (at 300 ppm). This was estimated by simulating the evolution of the longitudinal magnetization at the center of k-space taking account of the readout pulses and delays in the sequence; for white matter the longitudinal magnetization at that point was found to be 0.76 *Mo* for the SS sequence and 0.82 *Mo* for the PS sequence. A constant scan time and a noise level of 1% *Mo* was assumed for both SS and PS. A similar expression can be written for NOE. The effect of RF inhomogeneity on the saturation was characterized using:

$$SL = \left(\frac{S(B_1 = 100\%) - S(B_1 = 60\%)}{S(B_1 = 100\%)}\right) \times 100 \qquad [4]$$

where S is the saturation at different fractions of the expected amplitude of B1.

Data Acquisition

The study was approved by the local ethics committee of the University of Nottingham Medical School and all of volunteers gave informed consent. All experiments were performed on a 7 Tesla (T) Achieva MR system (Philips, Best, The Netherlands) using a quadrature transmit coil with a 32-channel-receive head coil (NOVA medical). Five healthy, consented, subjects were scanned using two CEST protocols at three nominal B1 amplitudes (1 μT, 2 μT, and 3 μT). The SS CEST protocol was as follows (11): saturation prepulse (a single RF-spoiled 25-ms sinc-gauss pulse followed by a 50-mT/m spoiler of 10 ms) interleaved with a sagittal, segmented EPI readout (EPI factor 13 with a binomial RF pulse for water only excitation), TR/echo time (TE)/FA = 58 ms/6 ms/10°, center of k-space weighted acquisition, the k-space center is measured at 8.8 s, time per volume 16.9 s, total scan time for z-spectrum 10 min 27 s. An FA of 10° for SS was chosen as approximately the Ernst angle.

The PS protocol was as follows (14): saturation prepulse (a train of 40 RF-spoiled 25 ms sinc-gauss pulses interleaved with a sinusoidal-modulated GR-spoiler, duty cycle 50%); readout (axial acquisition, three-shot TFE, TFE factor of 550, intershot interval 2 s, TR/TE/FA = 2.3 ms/1.05 ms/10°, phase encoding spirals out from the center of k-space in y–z); two dummy scans, time per volume 15.9 s, scan time 10 min 18 s. An FA of 10° for PS was chosen as a trade-off between sensitivity and point spread function. The parameters for both sequences were chosen to match the total acquisition scan times as closely as possible. In both cases, the field of view (FOV) was 150 × 224 × 208 mm^3 and the voxel size was 2 mm isotropic with SENSE factor 2. Second-order shimming was applied to improve the homogeneity of the magnetic field across the whole brain. The CEST spectra were sampled at 37 frequency offsets (Hz): 0, ±25, ±75, ±150, ±300, -500, -550, ±600, -675, ±800, 850, ±900, 960, 1020, -1050, 1080, 1140, ±1200, 1260, ±1500, ±1560, ±1600 (scans were also acquired at ±100 kHz relative to the water frequency for normalization). A T1-weighted anatomical image was used to produce white matter (WM) and gray matter (GM) masks. A B1 map was acquired based on a dual TR sequence (19) and subsequently scaled to reflect the ratio between actual B1+ and nominal B1+. For SNR estimations, a noise image was obtained by switching off all of RF pulses and gradients.

Data Processing

CEST data were coregistered to the mean volume in FSL [FMRIB v6.0, UK, FLIRT (20,21)]. For region of interest (ROI) positioning, a B1 map was overlaid on a WM mask. Three small ROIs (100 mm^2) were placed on a B1 map in different WM brain regions with B1 values at approximately 70%, 80%, and 100% of the nominal value (Fig. 2). For the three nominal B1 amplitudes, these three gave ROIs for nine actual B1 values of 0.7 μT, 0.8 μT, 1.0 μT, 1.4 μT, 1.6 μT, 2.0 μT, 2.1 μT, 2.4 μT, and 3.0 μT. Before the averaging, each spectrum in the ROI was B0-corrected pixel-wise by estimating the minimum of CEST spectrum (spline interpolated to a resolution of 1 Hz) and shifting the whole z-spectrum accordingly (22). CEST spectra from these ROIs were used to estimate APT and NOE effect sizes (termed APT* (Eq. [5]) and NOE* (Eq. [6])) using the three-point method which is an approximation because it assumes a linear baseline (23):

$$APT* = \left(\frac{\mathrm{Mz}(3.0\mathrm{ppm}) + \mathrm{Mz}(4.0\mathrm{ppm})}{2}\right) - \mathrm{Mz}(3.5\mathrm{ppm}) \qquad [5]$$

$$NOE* = \left(\frac{\mathrm{Mz}(-5.0\mathrm{ppm}) + \mathrm{Mz}(-2.0\mathrm{ppm})}{2}\right) - \mathrm{Mz}(-3.5\mathrm{ppm}) \qquad [6]$$

To compare the sensitivity of the sequences, we have estimated the APT or NOE effect size relative to noise (SNRAPT* and SNRNOE*). This was derived by standard error propagation through Eq. [5] to give:

$$SNR_{APT*} = \frac{APT*}{\sqrt{1.5}Noise} \qquad [7]$$

where *Noise* is the standard deviation in the measured value of Mz (assumed to be the same at all frequency offsets). A similar expression can be formed for SNRNOE*.

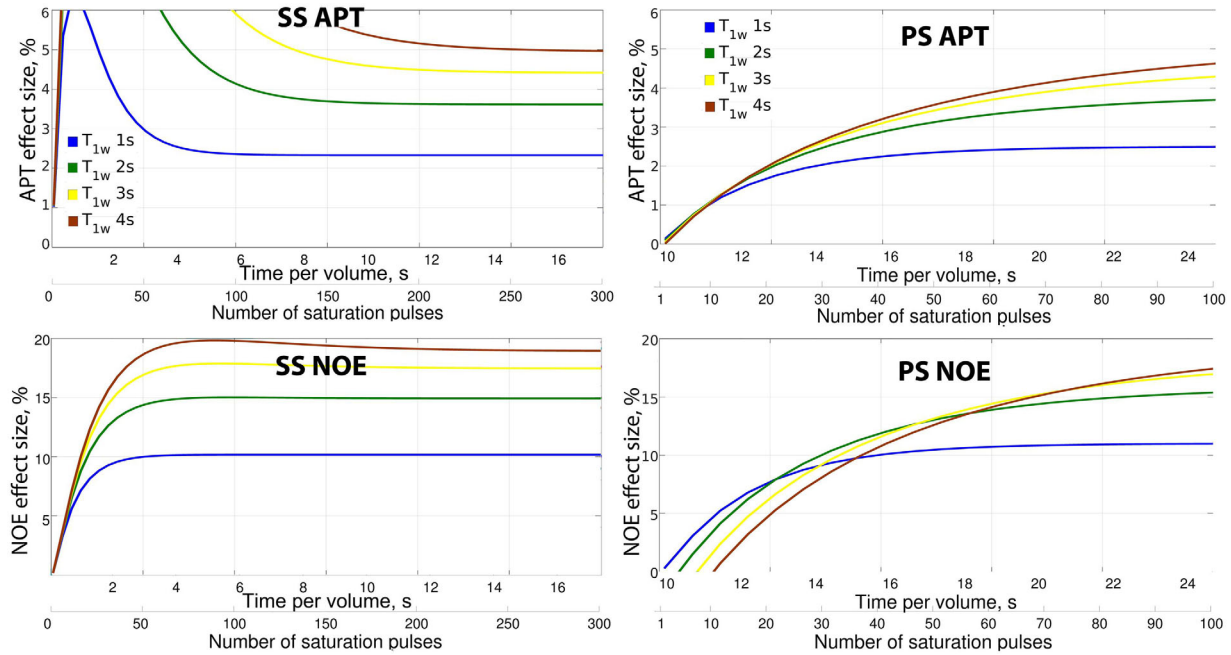

FIG. 3. Bloch-McConnell equations were used to simulate the APT and NOE contributions for SS and PS during the approach to SS, as a function of the number of saturation pulses (also recalculated as time-per-volume or dynamic scan time on the second axis) at a B_1 of 1 μT and various water-T_1 relaxation times. The frequency offsets used were 3.5 ppm and -3.5 ppm for APT and NOE, respectively.

All the simulations, data processing (apart from motion correction and anatomical image segmentation) and analysis were done in MATLAB (The Mathworks Inc., Natick, MA). A t-test was performed using the statistics toolbox in MATLAB to compare the data at the 5% significance level. The statistical comparison between SS and PS was made at the three nominal B1 levels: 1 μT, 2 μT, and 3 μT (pooling data across the different ROIs at each nominal value and across subjects).

RESULTS

Numerical Simulations

Figure 3 shows the simulated variation in APT and NOE signals during the approach to SS for increasing number of saturation pulses (also recalculated as time-per-volume, note the double axes) for different values of T1w, for both the SS and PS sequences. It is important to note that the number of saturation pulses corresponds to the number of TR repeats for SS and the number of pulses in a train of pulses for PS. As expected, for longer T1w more saturation pulses are required to reach the SS. The tissue T1w in the healthy human brain can vary between 1.1 s and 2.2 s for WM and cortical GM, respectively (24,25). Therefore, the number of saturation pulses for SS (Figure 3, left) was chosen to be 152 (or 8.8 s to reach the center of k-space, corresponding to minimum time-per-volume of 16.9 s), where both APT and NOE effects approximately plateau in both WM and GM. The number of saturation pulses for PS (Figure 3, right), was chosen to be 40 (or 15.9 s for time-per-volume), because at that point both APT and NOE effects are within 25% of their maxima for WM and GM. For the PS sequence, increasing the number of saturation pulses increases the scan length and, therefore, limits the number of points at which the z-spectrum can be sampled (spectral resolution) for a fixed scan time.

The chosen saturation pulse parameters were used in the subsequent simulations to determine the B1 amplitude and duty cycle providing maximum sensitivity to APT and NOE effect sizes (Fig. 4). For the SS sequence (Figure 1, top), the duty cycle is defined as the ratio of the time required for the presaturation to TR, whereas for the PS sequence (Figure 1, bottom), the duty cycle is just determined by the interpulse delay for the train of presaturation pulses. The SS scheme was found to give maximum APT effect size (Eq. [1]) (Figure 4, top left) at a B1 of 1 μT and 43% duty cycle (maximum allowed for the imaging readout used here) and maximum NOE effect size (Eq. [1]) (Figure 4, bottom left) at a B1 of 2 μT and 43% duty cycle (maximum allowed for the imaging readout used here); whereas PS scheme gave maximum APT effect size (Figure 4, top right) at a B1 of 1 μT and 50% duty cycle and maximum NOE effect size (Figure 4, bottom right) at a B1 of 2 μT and 50% duty cycle. The optimum duty cycle was largely insensitive to the number of saturation pulses for both sequences (not shown).

The effect size shown in Figure 4 is greater for the SS sequence than the PS sequence but it is the sensitivity (SNR in a constant time, Eq. [2]) that must be considered. Figure 5 compares variation in APT and NOE SNR with B1 amplitude, for the SS and PS sequences chosen to maximize APT and NOE effects sizes using the saturation parameters derived above. In the simulations, PS is more sensitive to APT and NOE effects at all power levels.

For the optimum saturation powers (1 μT and 2 μT for APT and NOE, respectively), both SS (43% duty cycle)

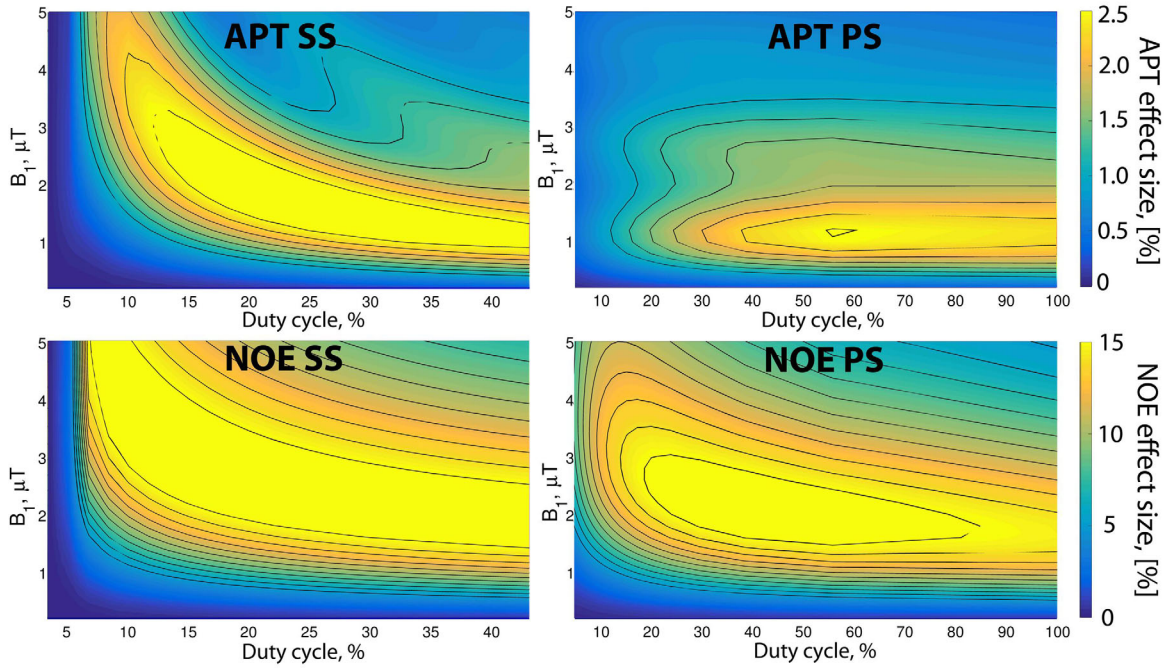

FIG. 4. The simulated 3D plots of APT and NOE effect sizes for SS and PS versus B_1 amplitude and duty cycle. The optimum saturation pulse parameters were determined from Figure 2. The simulated plots are overlaid with the contour lines to delineate the regions of the same signal intensity. The step size was 0.2 μT for B_1 and 1% for duty cycle.

and PS (50% duty cycle) demonstrated similar sensitivity to B1 inhomogeneity (Fig. 5). For a B1 dropout of 40%, the saturation loss (Eq. [4]) and the change in SNR (Eq. [2]) were found to be 6% and 35%, respectively, for APT, and 20% and 15%, respectively, for NOE, for both sequences. These results suggest that NOE effect is less sensitive to the transmit field inhomogeneity than APT.

In Vivo Studies

Figure 6 shows examples of spectra acquired with both methods. The raw images acquired at 3.5 ppm (APT offset) and -3.5 ppm (NOE offset) using both SS and PS schemes at 1 μT, 2 μT, and 3 μT are shown in Figure 7. The visual inspection of the raw images shows that WM/GM contrast is enhanced from 1 μT to 3 μT due to the B1-dependent MT effect. This is clearly seen in the normalized images (Fig. 7), which show similar amount of overall MT contrast present per saturation power in SS and PS images.

In Figure 8, the SNRAPT* and SNRNOE* measured in the ROIs indicated in Figure 2 and averaged over the subjects are plotted against actual B1 for both SS and PS schemes. SS and PS have maximum sensitivity to APT and NOE effects at relatively low B1 of 0.7–1.0 μT, and at this low power PS is more sensitive to APT and NOE than SS ($P < 0.05$). This is also reflected in the error bars of Z-spectra acquired at an actual B1 of 0.7 μT (Fig. 6).

DISCUSSION

In this work, we compared two pulsed 3D acquisition techniques that have been proposed for high resolution CEST imaging in the literature: an SS and a PS CEST image acquisition for the same brain coverage, scan time and spatial and spectral resolution. Both sequences were optimized for maximum sensitivity to APT and NOE effect sizes by varying the number of saturation pulses, transmit field amplitude, and duty cycle in simulations based on Bloch-McConnell equations. The optimized sequences were then compared on the basis of sensitivity

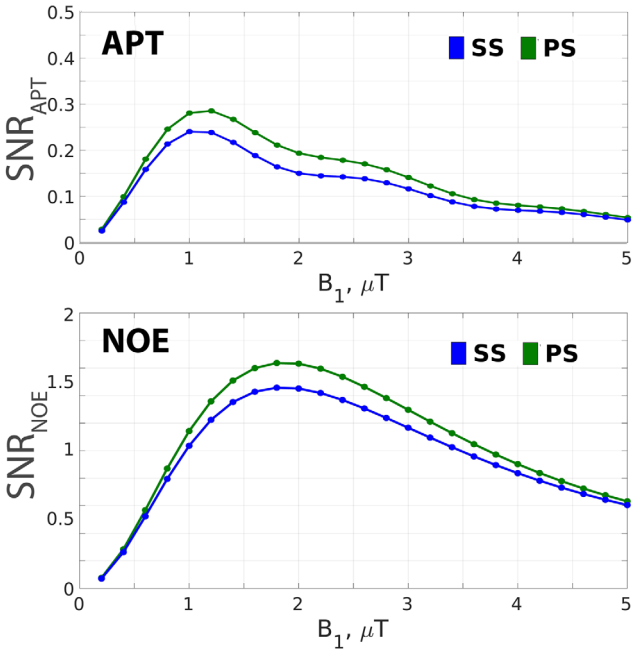

FIG. 5. The simulated B_1 dependence of SNR for APT (top) and NOE (bottom) effects for both SS and PS schemes. The step size for B_1 was 0.2 μT.

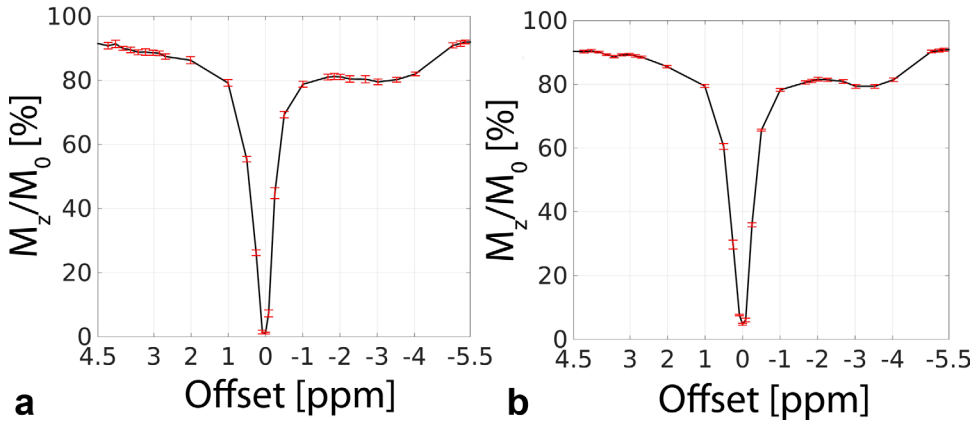

FIG. 6. Representative Z-spectra from a healthy volunteer for SS scheme (**a**) and PS scheme (**b**) acquired at an actual B_1 of 0.7 μT (ROI 1 in the Figure 2).

(SNR/time) to APT and NOE effects, and to transmit field inhomogeneity. According to the simulations, PS is more sensitive to both APT and NOE effects at all power levels simulated. Both acquisition schemes have similar dependence on the transmit field inhomogeneity. Experimental data confirm that PS has superior sensitivity to APT and NOE effects compared with SS at low power levels.

Numerical Simulations

SS CEST image acquisition

SS scheme comprises a short single pulse for saturation followed by a segmented 3D EPI readout with a short TR, producing low saturation efficiency due to an intrinsically low duty-cycle. Multiple sequence repetitions are required to build up the SS and data acquisition starts at a high frequency end of k-space so that the SS has been established by the time the center of k-space is reached. In vivo APT effect size is on the order of 1%, so the signal instability must be less than 1%. The rate at which the SS is reached is determined by T1w and the SS scheme must be optimized taking account of the maximum tissue T1w. For the normal healthy brain where tissue T1w can be as high as 2.2 s (25), stability is reached in ca. 8.8 s (or 152 TR repeats, corresponding to minimum time-per-volume of 16.9 s). However, the effect of T1w on the rate of reaching SS is an important factor to consider especially in tumors (26,27) where T1w can be longer.

Because saturation and image acquisition are interleaved in SS scheme, highest duty cycle is limited by the need for an image readout period. The maximum possible sensitivity to APT (Figure 4, top left) and NOE (Figure 4, bottom left) effect size for the maximum 43% duty cycle simulated here, was found to be for B1 of 1 μT and 2 μT, respectively. This result is in line with the literature. For this sequence, the maximum APT effect size was previously predicted to occur at a B1 of 1 μT (12), experiments later confirmed this (28), and only

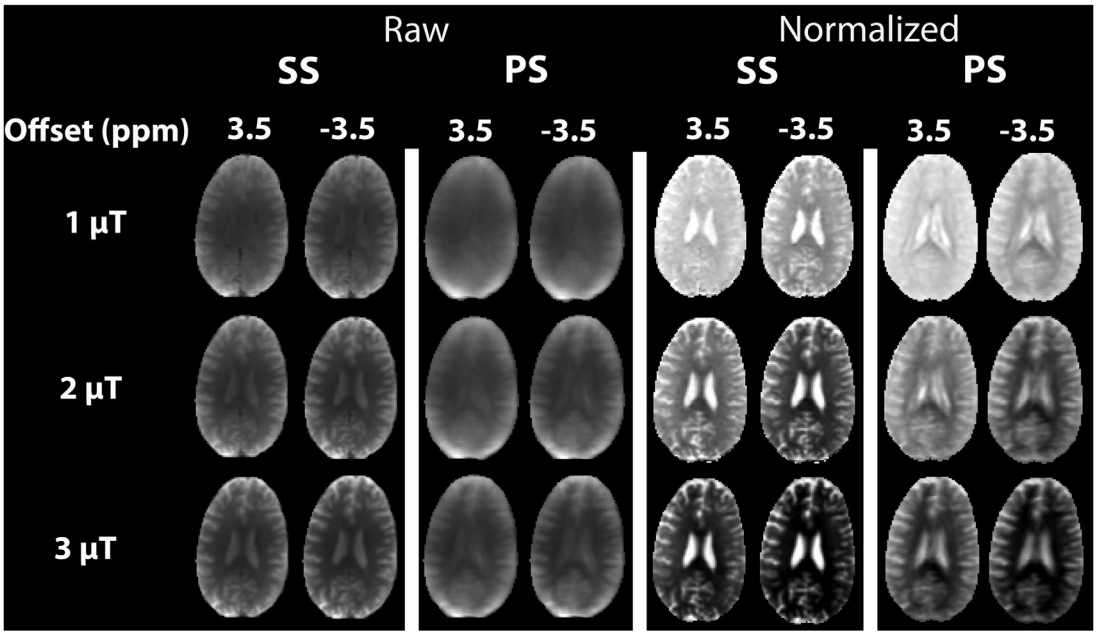

FIG. 7. SS and PS raw images (±3.5 ppm) and same images normalized by the corresponding reference scans at 300 ppm (scaled between 0.5 and 1) of a healthy brain acquired at three nominal B_1 levels: 1 μT, 2 μT, and 3 μT.

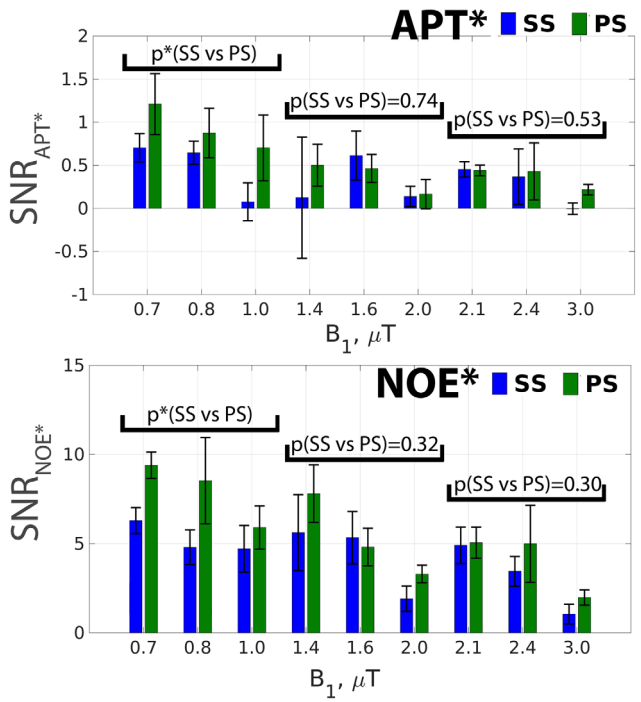

FIG. 8. The experimentally measured variation in APT* and NOE* SNR on B_1 level for both SS and PS schemes. The error bars represent standard deviation across five subjects. The SNR between the SS and PS sequences was compared by combining results for the nominal B_1 values for all five subjects.

found a marginal change in NOE effect size between B1 levels of 0.9, 1.4, and 1.9 μT (28).

A stronger main magnetic field is advantageous for CEST due to enhanced chemical shift dispersion, longer relaxation times and increased SNR, but transmit field inhomogeneity also increases with field strength. Figure 5 shows that at optimum power the sensitivity to exact B1 amplitude is quite low.

PS CEST image acquisition

The PS scheme comprises a train of saturation pulses and a segmented 3D TFE readout and an intershot delay of 2 s for signal recovery. Because a saturation train of a few seconds (typically 5 × T1w) is required to reach the SS, the total scan time can be reduced by acquiring the images in the PS by optimizing the number of saturation pulses, number of TFE shots and an intershot delay. In this work, we chose to match FOV spatial/spectral resolution and the total scan time of the PS and SS acquisitions. The number of pulses in the train of saturation pulses was chosen to maximize APT and NOE effects. Because the maximum tissue T1w in the healthy human brain can be as high as 2.2 s (25), near-optimum APT and NOE effects are reached in 40 pulses (or 15.9 s for time-per-volume). Three TFE shots are required to reach the PS and an intershot delay of 2 s was introduced for signal recovery to increase SNR.

Similar to the SS acquisition scheme (Fig. 4), maximum sensitivity to the effect size of APT (Figure 4, top right) and NOE (Figure 4, bottom right) was found at 50% duty cycle and a B1 of 1 μT and 2 μT, respectively. This duty cycle dependence of APT and NOE effects can be explained by the signal evolution during the mixing time (a delay between the saturation pulses in a train of pulses) (29). The rate of APT and NOE signal build-up during the mixing time depends on the exchange rate of the labile protons and T1w. For the optimum CEST prepulse parameters, both SS and PS have similar dependence on the transmit field inhomogeneity effects (Fig. 5).

In Vivo Studies

The three point analysis method is very sensitive to noise (because it involves none of the smoothing inherent in alternative fitting approaches); therefore, in this work we have only considered ROI analysis. There is reasonably good agreement between the simulations (Fig. 5) and the experiments (Fig. 8) for APT sensitivity which is maximum at relatively low B1. At this low power level (0.7–1.0 μT), PS has superior sensitivity to both APT and NOE effects. This can also be seen in the error bars of Z-spectra acquired at a B1 of 0.7 μT using both sequences (Fig. 6). Both APT and NOE effects are considered to be in the slow exchange regime and whether the results are applicable to the other metabolites containing faster exchanging protons, e.g., amine and hydroxyl, requires a further investigation. The experimental SNR for NOE exceeded the simulated prediction, suggesting errors in the parameters or numbers of pools assumed in the simulation, including possible MT asymmetry (6,11,14,30,31), and the use of the approximate three-point model to fit the data. The correlation coefficient (R) between the sequences was found to be 0.84 and 0.92, for APT and NOE SNR, respectively (Fig. 8). This suggests that the sequences have similar sensitivity to the effects of transmit field inhomogeneity.

The scan time for the SS scheme is limited by the amount of time it takes to reach the SS, which is in turn dictated by water T1w. Therefore, SS is limited to only 3D acquisitions because it needs to have enough phase-encoding steps to establish the SS. On the other hand, the PS scheme is more flexible due to the potential trade-off between the saturation level (number of saturation pulses), brain coverage and spatial and spectral resolution. This trade-off is assisted by its inherently greater SNR, due to the delay for T1 recovery in between each shot in multishot TFE readout.

In this work Figure 7. shows that the PS images are blurry compared with those of SS due to the variation in signal during the TFE readout (14). A shorter TFE readout combined with a longer TR would sharpen the PSF, but would also reduce the FOV by decreasing the number of phase encoding steps per TFE readout for a fixed scanning time. For instance, we have previously reported a spatial resolution of 0.4 mm^2 with an excellent image quality over a smaller volume using this sequence (14). The blurring could be compensated for by increasing the number of readout shots and consequently the scan length or alternatively by reducing the readout FA. Another advantage of PS acquisition scheme is that the mixing time between the pulses used for labelling exchangeable protons can be readily modified, giving a potential duty cycle of 0–100%. As a result of this

flexibility the sequence can be sensitized to labile protons with a specific exchange rate for instance using the variable delay multipulse CEST approach (29,32). The sharpness in SS images can also be affected by EPI distortions. In this work, we chose to match SS and PS in terms of brain coverage, spectra resolution, and the total scan time, but other features such as image sharpness could be investigated as well.

CONCLUSIONS

In this report, SS and PS pulsed 3D CEST acquisition schemes were compared at 7T in terms of the sensitivity to APT and NOE, and to transmit field inhomogeneity for the same brain coverage, spatial/spectral resolution and scan time. Bloch-McConnell equation simulations were used to investigate the effects of the number of saturation pulses, transmit field amplitude, and duty cycle, to optimize both sequences for maximum sensitivity to the effect size of APT and NOE. The results of this study suggest that PS is superior to SS in terms of sensitivity for the imaging of the slow chemical exchange mediated processes at low power levels. Both acquisition schemes were found to have similar sensitivity to transmit field inhomogeneity effects.

REFERENCES

1. Guivel-Scharen V, Sinnwell T, Wolff SD, Balaban RS. Detection of proton chemical exchange between metabolites and water in biological tissues. J Magn Reson 1998;133:36–45.
2. Vinogradov E, Sherry AD, Lenkinski RE. CEST: from basic principles to applications, challenges and opportunities. J Magn Reson 2013; 229:155–172.
3. Zhou J, Lal B, Wilson DA, Laterra J, van Zijl PC. Amide proton transfer (APT) contrast for imaging of brain tumors. Magn Reson Med 2003;50:1120–1126.
4. Jones CK, Schlosser MJ, van Zijl PCM, Pomper MG, Golay X, Zhou J. Amide proton transfer imaging of human brain tumors at 3T. Magn Reson Med 2006;56:585–592.
5. Zhou J, Blakeley JO, Hua J, Kim M, Laterra J, Pomper MG, van Zijl PC. Practical data acquisition method for human brain tumor amide proton transfer (APT) imaging. Magn Reson Med 2008;60:842–849.
6. Zhou J, Payen JFF, Wilson DA, Traystman RJ, van Zijl PC. Using the amide proton signals of intracellular proteins and peptides to detect pH effects in MRI. Nat Med 2003;9:1085–1090.
7. Sun PZ, Zhou J, Sun W, Huang J, van Zijl PCM. Detection of the ischemic penumbra using pH-weighted MRI. J Cereb Blood Flow Metab 2006;27:1129–1136.
8. Jokivarsi KT, Gröhn HI, Gröhn OH, Kauppinen RA. Proton transfer ratio, lactate, and intracellular pH in acute cerebral ischemia. Magn Reson Med 2007;57:647–653.
9. Paech D, Burth S, Windschuh J, et al. Nuclear overhauser enhancement imaging of glioblastoma at 7 Tesla: region specific correlation with apparent diffusion coefficient and histology. PloS One 2015;10: e0121220.
10. Zhang XY, Xie J, Xu J, Li H, Gore JC, Zu Z. Assessment of membrane fluidity using nuclear overhauser enhancement mediated magnetization transfer (NOE-mediated MT). In Proceedings of the 23rd Annual Meeting of ISMRM, Toronto, Canada, 2015. Abstract 1747.
11. Liu G, Ali MM, Yoo B, Griswold MA, Tkach JA, Pagel MD. PARACEST MRI with improved temporal resolution. Magn Reson Med 2009; 61:399–408.
12. Jones CK, Polders D, Hua J, Zhu H, Hoogduin HJ, Zhou J, Luijten, P, van Zijl PC. In vivo three-dimensional whole-brain pulsed steady-state chemical exchange saturation transfer at 7 T. Magn Reson Med 2012;67:1579–1589.
13. Zhu H, Jones CK, van Zijl PCM, Barker PB, Zhou J. Fast 3D chemical exchange saturation transfer (CEST) imaging of the human brain. Magn Reson Med 2010;64:638–644.
14. Mougin O, Clemence M, Peters A, Pitiot A, Gowland P. High-resolution imaging of magnetisation transfer and nuclear Overhauser effect in the human visual cortex at 7 T. NMR Biomed 2013;26:1508–1517.
15. McConnell HM. Reaction rates by nuclear magnetic resonance. J Chem Phys 1958;28:430–431.
16. Woessner DE, Zhang S, Merritt ME, Sherry AD. Numerical solution of the Bloch equations provides insights into the optimum design of PARACEST agents for MRI. Magn Reson Med 2005;53:790–799.
17. Ramani A, Dalton C, Miller DH, Tofts PS, Barker GJ. Precise estimate of fundamental in-vivo MT parameters in human brain in clinically feasible times. J Magn Reson Imaging 2002;20:721–731.
18. Sun PZ, Lu J, Wu Y, Xiao G, Wu R. Evaluation of the dependence of CEST-EPI measurement on repetition time, RF irradiation duty cycle and imaging flip angle for enhanced pH sensitivity. Phys Med Biol 2013; 58:N229–N240.
19. Yarnykh VL. Actual flip-angle imaging in the pulsed steady state: a method for rapid three-dimensional mapping of the transmitted radiofrequency field. Magn Reson Med 2007;57:192–200.
20. Jenkinson M, Smith S. A global optimisation method for robust affine registration of brain images. Med Image Anal 2001;5:143–156.
21. Jenkinson M, Bannister P, Brady M, Smith S. Improved optimization for the robust and accurate linear registration and motion correction of brain images. Neuroimage 2002;17:825–841.
22. Kim M, Gillen J, Landman BA, Zhou J, van Zijl PC. Water saturation shift referencing (WASSR) for chemical exchange saturation transfer (CEST) experiments. Magn Reson Med 2009;61:1441–1450.
23. Jin T, Wang P, Zong X, Kim SG. MR imaging of the amide-proton transfer effect and the pH-insensitive nuclear overhauser effect at 9.4 T. Magn Reson Med 2013;69:760–770.
24. Wright PJ, Mougin OE, Totman JJ, et al. Water proton T1 measurements in brain tissue at 7, 3, and 1.5T using IR-EPI, IR-TSE, and MPRAGE: results and optimization. MAGMA 2008;21:121–130.
25. Rooney WD, Johnson G, Li X, Cohen ER, Kim SG, Ugurbil K, Springer CS. Magnetic field and tissue dependencies of human brain longitudinal 1H2O relaxation in vivo. Magn Reson Med 2007;57:308–318.
26. Zaiss M, Windschuh J, Paech D, et al. Relaxation-compensated CEST-MRI of the human brain at 7T: unbiased insight into NOE and amide signal changes in human glioblastoma. Neuroimage 2015;112:180–188.
27. Khlebnikov V, Polders D, Hendrikse J, Robe PA, Voormolen EH, Luijten PR, Klomp DW.J, Hoogduin H. Amide proton transfer (APT) imaging of brain tumors at 7 T: the role of tissue water T1-relaxation properties. Magn Reson Med 2017;77:1525–1532.
28. Liu D, Zhou J, Xue R, Zuo Z, An J, Wang DJJ. Quantitative characterization of nuclear verhauser enhancement and amide proton transfer effects in the human brain at 7 tesla. Magn Reson Med 2013;70:1070–1081
29. Xu J, Yadav NN, Bar-Shir A, Jones CK, Chan KW, Zhang J, Walczak P, McMahon MT, van Zijl PC. Variable delay multi-pulse train for fast chemical exchange saturation transfer and relayed-nuclear overhauser enhancement MRI. Magn Reson Med 2014;71:1798–1812.
30. Mougin OE, Coxon RC, Pitiot A, Gowland PA. Magnetization transfer phenomenon in the human brain at 7 T. Neuroimage 2010;49:272–281.
31. Liu D, Zhou J, Xue R, Zuo Z, An J, Wang DJJ. Quantitative characterization of nuclear overhauser enhancement and amide proton transfer effects in the human brain at 7 tesla. Magn Reson Med 2013;70:1070–1081.
32. Xu X, Yadav NN, Zeng H, Jones CK, Zhou J, van Zijl PCM, Xu J. Magnetization transfer contrast–suppressed imaging of amide proton transfer and relayed nuclear overhauser enhancement chemical exchange saturation transfer effects in the human brain at 7T. Magn Reson Med 2016;75:88–96.